MATERIALS CHEMISTRY FRONTIERS

RESEARCH ARTICLE

View Article Online
View Journal | View Issue

Cite this: *Mater. Chem. Front.*, 2026, **10**, 1603

A simple and cost-effective thiophene–benzene–thiophene-based hole transporting material for stable perovskite solar cells

Nousheen Syed,†[a] Ankita Sharma,†[b] Thillaiarasi Sukumar,[a] Ganesh Koyyada,[c] David Kreher,[d] Baswanth Oruganti,[e] Upendra Kumar Pandey *[b] and Kamatham Narayanaswamy *[a]

Received 26th October 2025,
Accepted 27th February 2026

DOI: 10.1039/d5qm00763a

rsc.li/frontiers-materials

The efficiency and stability of perovskite solar cells (PSCs) are often constrained by the limitations of the conventional hole transporting material (HTM), Spiro-OMeTAD, which exhibits low intrinsic conductivity, poor thermal endurance, dopant-induced instability and high synthetic cost. In this work, two low-cost HTMs, **NS-1** and **NS-2**, were designed and synthesized *via* a facile process. Both materials share a common thiophene–benzene–thiophene (TBT) conjugated core with triarylamine terminal groups but differ in their side chains: **NS-1** contains methoxy ($-OCH_3$) substituents, whereas **NS-2** incorporates polar ethylene glycol moieties on the TBT unit. These HTMs were synthesized through a cost-effective route, with material costs of \$35 per g and \$37 per g for **NS-1** and **NS-2**, respectively, lower than that of the commercially available Spiro-OMeTAD (~\$333 per g). The influence of side-chain engineering on their optical, electrochemical, photophysical, charge-transport, and photovoltaic properties was systematically investigated. Among the two, **NS-2** exhibited superior molecular planarity, enhanced hole mobility and better energy-level alignment, leading to an impressive power conversion efficiency (PCE) of 17.50%, compared to 4.96% for **NS-1**, which suffered from poor solubility and non-uniform film formation. Moreover, **NS-2**-based devices retained 84% of their initial efficiency after 1200 hours of operation, surpassing Spiro-OMeTAD in stability. The combination of high efficiency, long-term stability and low-cost synthesis establishes **NS-2** as a promising HTM for scalable PSCs.

1. Introduction

Over the past decade, perovskite solar cells (PSCs) have gained significant attention due to their rapidly improving power conversion efficiency (PCE), which has now reached 27%.[1,2] Among the essential components of PSCs, hole transporting materials (HTMs) are crucial for extracting photogenerated holes and suppressing carrier recombination.[3] The HTM plays a pivotal role in PSCs, as it facilitates selective extraction and transport of photogenerated holes to the anode while blocking electrons, thereby suppressing interfacial recombination.

In the conventional n–i–p architecture, a typical device structure comprises a transparent conducting oxide, an electron transport layer, an intrinsic perovskite absorber, a HTM layer, and a metal electrode. Significant progress in the device efficiency of PSCs has been driven by the development of new HTMs.[4,5] Various types of HTMs have been employed in n–i–p PSC architectures, broadly categorized into organic small molecules (*e.g.*, Spiro-OMeTAD),[6,7] conductive polymers (*e.g.*, PEDOT:PSS, P3HT and PTAA),[8] and inorganic materials (*e.g.*, NiO, CuSCN, and CuI).[9] Each class offers distinct advantages in terms of energy-level alignment, film formation, and stability. Still, to date Spiro-OMeTAD remains the benchmark HTM for high-performance PSCs.[4]

Spiro-OMeTAD offers advantages such as a stable amorphous morphology from its relatively high glass-transition temperature (T_g)[10] and favourable energy-level alignment with the perovskite absorber, good film-forming ability and ability to achieve high device efficiency by effectively extracting holes.[11] However, its practical use is hindered by low intrinsic

[a] *Department of Chemistry, SRM University-AP, Amaravati, Andhra Pradesh, 522240, India. E-mail: kamatham.n@srmap.edu.in*
[b] *Organic & Flexible Electronics Laboratory, Department of Electrical Engineering, School of Engineering, Shiv Nadar Institution of Eminence, G.B. Nagar, Uttar Pradesh-201314, India. E-mail: upendra.pandey@snu.edu.in*
[c] *School of Chemical Engineering, Yeungnam University, Daehak-ro 280, Gyeongsan, Gyeongbuk 38541, South Korea*
[d] *Institut Lavoisier de Versailles, UMR CNRS 8180, UVSQ, Université Paris-Saclay, Versailles, 78035, France*
[e] *School of Mathematics and Mathematical Statistics, Umeå University, SE-90187, Umeå, Sweden*
† These authors contributed equally to this work.

conductivity and hole mobility, necessitating dopants such as lithium bis(trifluoromethylsulfonyl)imide (Li-TFSI) and 4-*tert*-butylpyridine (*t*BP) or cobalt complexes like FK209, all highly hygroscopic.[12,13]

These dopants induce moisture sensitivity, ion migration, hysteresis, interfacial instability, and accelerated degradation during operation.[14] In addition, its high synthetic cost makes it one of the most expensive components in PSCs limiting large-scale commercialization.[11]

These challenges have motivated extensive research into alternative HTMs that are more stable, cost-effective and capable of efficiently transporting holes while maintaining device performance and long-term stability. The operational instability caused by hygroscopic dopants, coupled with the high material cost, has prompted researchers to explore alternative HTM materials that offer enhanced environmental stability, scalability and cost effectiveness without compromising efficiency.

Among the different classes of HTMs, π-conjugated organic small-molecular HTMs stand out for their well-defined molecular structures, excellent reproducibility and precisely tunable optoelectronic properties.[15] Typically, the solution-processable conjugated materials comprise two components: a π-conjugated backbone that governs the molecule's optoelectronic properties and peripheral flexible side chains that impart solubility.[16] The selection of side chains is as critical as conjugated backbones itself.[17] Alkyl chains not only enable solution processing but also influence molecular packing and consequently, the optoelectronic performance of the material.[16]

Building on this, researchers have gone beyond simple alkyl substitution and explored a variety of functional side chains to tailor both solubility and device performance. Conjugated systems have also been functionalized with heteroatom-containing alkyl chains,[18] siloxane-terminated side chains,[19,20] fluoroalkyl groups,[21,22] oligo(ethylene glycol) chains,[23] and ionic side chains[18] to improve charge carrier mobilities.[23] Among these, the introduction of polar ethylene glycol side chains increases the polarity of the molecule, makes it easier to purify and enables green solvent processing.[24] Moreover, the introduction of ethylene glycol chains, imparts Lewis base characteristics, enabling it to coordinate with Pb^{2+} ions and suppress Li^{+} migration, thereby lowering environmental risks and enhancing long-term stability.[24] On the other hand, thiophene units are anticipated to enhance intermolecular interactions and promote π–π stacking, thereby contributing to the improved conductivity of HTMs.[25]

Several recent examples highlighted the potential of such strategies. For instance, Zhang *et al.* developed two dopant-free HTMs, DCT and DTC, incorporating intramolecular noncovalent interactions and simple synthesis routes; DCT with hexyloxy groups showed better planarity than DTC due to O···S interactions. PSCs employing DCT achieved a PCE of 22.5% along with long-term, light, and thermal stability.[26] Similarly, Ren *et al.* reported, a benzo[1,2-*b*:4,5-*b*′]dithiophene (BDT)-based HTM, BDT2FMeDPA, exhibiting enhanced hole mobility, conductivity and stability, delivering a PCE of 14.5%.[27] Furthermore, Li *et al.* introduced two HTMs, BTORA and BTORCNA, designed using an intramolecular noncovalent interaction (INI) strategy by introducing S···O interactions into their backbones. The resulting HTMs exhibited self-planarized backbones, tuned energy levels, improved thermal stability, favourable film morphology and effective defect passivation. Notably, BTORCNA-based devices achieved a PCE of 21.10% with higher long-term stability, outperforming BTORA-based devices without S···O interactions, demonstrating INIs as an effective route for developing dopant-free HTMs.[28]

Inspired by these advances, we designed and synthesized two new HTMs, **NS-1** and **NS-2** (Fig. 1), based on a well-established organic conjugated framework, thiophene–benzene–thiophene (TBT)[25] as a central building block, and triarylamine units as terminal electron-donating groups, both of which are commonly utilized in OPVs[29,30] and OLEDs.[31,32] While both HTMs share the same TBT core and are decorated with two triarylamine peripheral groups, they differ in the nature of the side chains attached to the TBT core: **NS-1** incorporates methoxy ($-OCH_3$) side chains, whereas **NS-2** features polar ethylene glycol side chains. **NS-1** was deliberately designed as a structurally matched reference molecule to decouple side-chain effects from backbone electronic properties. Although **NS-1** exhibits limited solubility and device applicability, its inclusion enables a controlled evaluation of how side-chain chemistry governs solubility, film formation, and interfacial charge transport within this HTM framework. A comprehensive investigation of their key properties, including optical absorption, thermal stability, electrochemical behaviour, photophysical characteristics, and electrical properties, was carried out, followed by evaluation of their photovoltaic performance in PSC devices.

2. Results and discussion

The detailed synthetic routes for **NS-1** and **NS-2** are illustrated in Fig. S1. Both HTMs were synthesized in five steps, with high overall yields from cost-effective and readily available starting materials through well-established cross coupling reactions and straightforward purification procedures. The overall synthetic yields for **NS-1** and **NS-2** were 20% and 43%, respectively. Based on established cost estimation models, their synthetic costs were calculated to be \$35 per g for **NS-1** and \$37 per g for **NS-2**, which are considerably lower than that of the commercially available Spiro-OMeTAD (~\$333 per g) (Table S9). In contrast, the synthesis of Spiro-OMeTAD typically involves multistep ring-closure reactions that often result in low yields and require harsh reaction conditions.[33] Comprehensive synthetic details and full characterization data for **NS-1** and **NS-2** are provided in the SI (Section 2).

2.1. Optical characterization

The optical and electrochemical properties of **NS-1** and **NS-2** are summarized in Table 1, and their ultraviolet-visible (UV-vis) absorption spectra recorded in $CHCl_3$ are shown in Fig. 2. Both

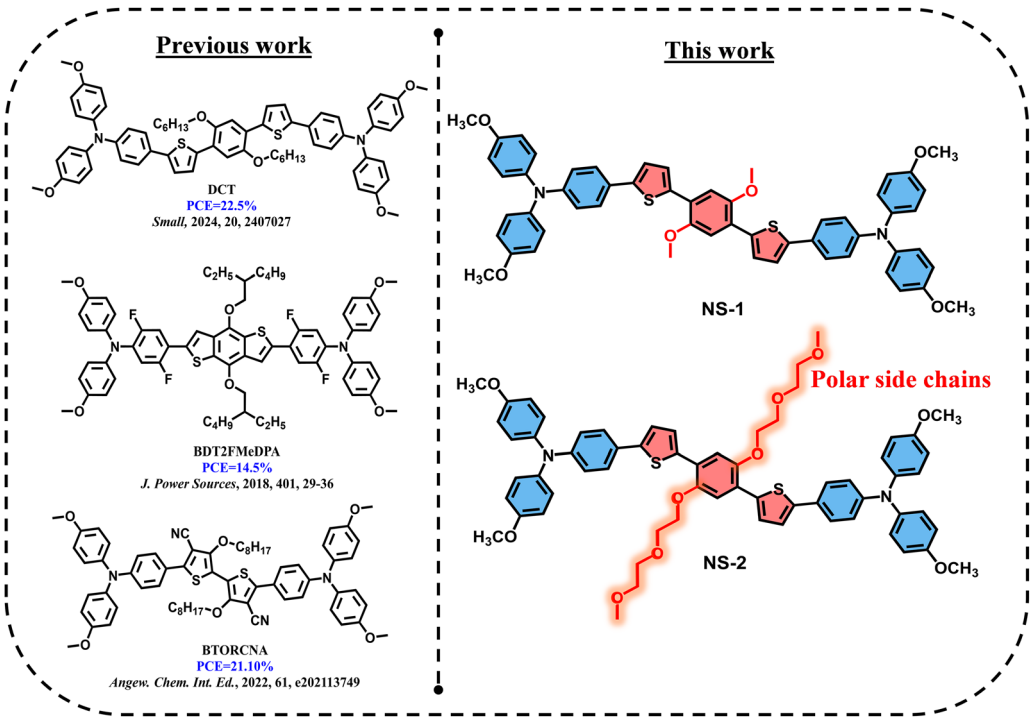

Fig. 1 Chemical structures of the representative molecular hole-transporting materials (HTMs) used in perovskite solar cells (PSCs), including DCT,[26] BDT2FMeDPA,[27] and BTORCNA[28] along with the HTMs **NS-1** and **NS-2** developed in this work.

Table 1 Optical, electrochemical, and thermal properties of **NS-1** and **NS-2**

HTMs	λ_{max} (nm) sol Exp.[a]	λ_{max} (nm) sol Theoretical[b] (CAM-B3LYP)	λ_{max} (nm)[c] Solid state	λ_{onset} (nm)[d] Sol	E_g^{opt} (eV)[e]	E_{HOMO} (eV)[f]	E_{LUMO} (eV)[g]	$T_d^{5\%}$ (°C)[h]	T_g (°C)[i]
NS-1	425	414	433	493	2.50	−4.95	−2.45	430	215
NS-2	426	413	436	494	2.50	−5.09	−2.59	409	146

[a] Measured in $CHCl_3$ solution at a concentration of 10^{-5} M. [b] Theoretical values for the **NS-1** and **NS-2** molecules. [c] Measured as a thin film. [d] Measured from the onset of UV-vis spectra in solution. [e] Calculated using the equation $E_g^{opt} = 1240/\lambda_{onset}$ (eV). [f] Calculated from the onset oxidation potentials using the equation $E_{HOMO} = -[E_{oxi} - E_{(Fc/Fc^+)} + 4.8]$ (eV); $E_{(Fc/Fc^+)} = 0.48$. [g] Calculated using the equation $E_{LUMO} = E_{HOMO} + E_g^{opt}$. [h] Calculated from TGA. [i] Calculated from DSC (with a scan rate of 10 °C min^{-1}; N_2 atmosphere).

HTMs exhibit similar absorption spectra in the visible region, with distinct absorption peaks at λ_{max} 425 nm for **NS-1** and λ_{max} 427 nm for **NS-2**, corresponding to the π–π* transitions of the π electron system.[34] In the solid state, both the HTMs display a pronounced red shift, indicating enhanced π–π stacking interactions.[35] Importantly, the relatively narrow absorption bands, below 450 nm are more advantageous for PSC application, as they minimize parasitic absorption from the HTM layer and thereby help preserve efficient light harvesting by the perovskite absorber. The optical bandgaps (E_g) of **NS-1** and **NS-2** were estimated from the thin-film absorption onset in the UV-vis spectra (Fig. 2) using the relationship $E_g^{opt} = 1240/\lambda_{onset}$ (eV), and were found to be 2.50 eV for both compounds (Table 1). While the optical bandgap governs the absorption characteristics of the HTM, efficient hole extraction is primarily determined by the alignment of the HTM's HOMO level with the valence band maximum of the perovskite. In this regard, the HOMO levels of **NS-1** and **NS-2** are well aligned with that of Spiro-OMeTAD, indicating energetically favourable hole extraction (Fig. 6b).

2.2. Electrochemical properties

To determine the energy levels of the two HTMs, cyclic voltammetry (CV) measurements (Fig. S2) were carried out in dichloromethane (DCM) containing 0.1 M tetrabutylammonium hexafluorophosphate (Bu_4NPF_6), as the supporting electrolyte. The corresponding energy levels are shown in Fig. 6b, and the relevant electrochemical data are summarized in Table 1.

The highest occupied molecular orbital (HOMO) energy levels were calculated with the calibrated onset oxidation (E_{onset}^{ox}) of CV using the equation:

$$E_{HOMO} = -[E_{oxi} - E_{(Fc/Fc^+)} + 4.8]\ (eV)$$

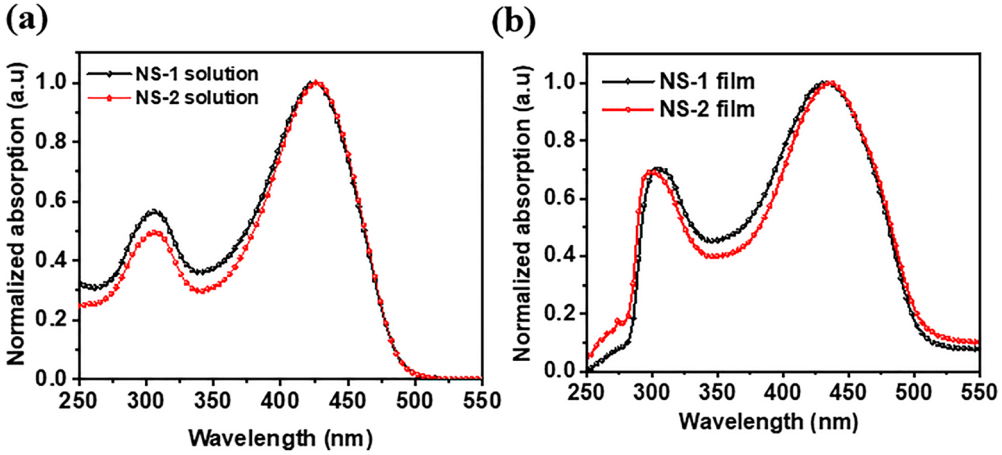

Fig. 2 Normalized absorption spectra of **NS-1** and **NS-2** in (a) $CHCl_3$ and the (b) solid state (spin-coated on a glass substrate).

The lowest unoccupied molecular orbital (LUMO) energy levels were calculated using the HOMO energy level (E_{HOMO}) and optical bandgap (E_g) using the equation:

$$E_{LUMO} = E_{HOMO} + E_g \text{ (eV)}$$

The results indicate that both **NS-1** and **NS-2** exhibit deeper HOMO energy levels (−4.95 eV and −5.09 eV, respectively), making them well-suited to serve as efficient hole extractors at the perovskite $(Cs_{0.05}(FA_{0.79}MA_{0.16})_{0.95}Pb(I_{0.77}Br_{0.23})_3)$/HTM interface. For **NS-1** and **NS-2**, the LUMO levels are −2.45 eV and −2.59 eV, respectively. Both the HTMs exhibit LUMO levels higher than the conduction band (CB) of the perovskite, indicating that the transfer of photogenerated electrons from the perovskite to the HTM layer is suppressed, thereby effectively reducing electron–hole recombination.[36]

2.3. Thermal properties

The thermal properties of **NS-1** and **NS-2** were investigated using thermogravimetric analysis (TGA) and differential scanning calorimetry (DSC), as depicted in Fig. S3. The TGA curve shows that both HTMs exhibit excellent thermal stability, with 5% weight loss (T_d) occurring above 400 °C under a nitrogen atmosphere (Fig. S3a). The glass transition temperatures (T_g) of **NS-1** and **NS-2** were determined to be 215 °C and 146 °C, respectively, reflecting good morphological stability. The higher T_g and T_d indicate that improved thermal stability could be expected.[37] Moreover, the absence of distinct melting peaks in the DSC curves (Fig. S3b) indicates that **NS-1** and **NS-2** are amorphous, which are higher enough for application in optoelectronic devices. The T_g values of **NS-1** and **NS-2** are higher than the T_g of Spiro-OMeTAD,[38] which may lead to better stability of the devices over time. This leads us to conclude that the overall thermal stability of **NS-1** and **NS-2** is better than the benchmark Spiro-OMeTAD. Thus, both **NS-1** and **NS-2** are also expected to be applicable as effective HTMs for PSCs.

2.4. Computational Studies

To further corroborate experimental findings and obtain deeper insights into the molecular structures, absorption properties and charge distribution of **NS-1** and **NS-2**, computational studies were performed using density functional theory (DFT) by employing the CAM-B3LYP and ωB97X-D hybrid density functionals. The optimized molecular geometries of **NS-1** and **NS-2** are presented in Fig. 3 and 4. Of particular interest are the dihedral angles C1–C2–C3–S4 and C1′–C2′–C3′–S4′ shown in Fig. 3a and 4a, which reflect the degree of planarity between the donor and acceptor units, and directly influence the conjugation length and, in turn, the optoelectronic properties of the molecules. For **NS-1**, the dihedral angles are 19° and 16°, respectively. Similarly, for **NS-2**, the corresponding values are 19° and 17°. The deviation from perfect planarity arises from steric repulsions between the hydrogen atoms of the thiophene and benzene units, adjacent to C2 and C3 atoms (or C2′ and C3′ atoms). Notably, the dihedral angles in **NS-1** and **NS-2** are nearly equal, despite the presence of a longer ethylene glycol side chain in **NS-2**, which can be rationalized in terms of orientation of this group, projecting away from the central TBT core.

Turning to the absorption properties of **NS-1** and **NS-2**, as can be noted from Table 1 and Fig. S5 of the SI, the λ_{max} values of 413–414 nm obtained using the CAM-B3LYP functional are in excellent agreement with corresponding experimental values (within 11–13 nm), while those obtained with the ωB97X-D functional have a relatively larger deviation. Moreover, the computed electrostatic surface potential (ESP) maps, shown in Fig. 3c and 4c, provide a visual representation of the charge distribution across the molecule, with red regions corresponding to the negative electrostatic potential (electron-rich sites) and blue regions corresponding to the positive electrostatic potential (electron-deficient sites). This distribution substantiates the donor–acceptor nature of these molecules.

2.5. Charge transport properties

After the preliminary characterization of **NS-1** and **NS-2**, their performance as hole transporting materials was evaluated in

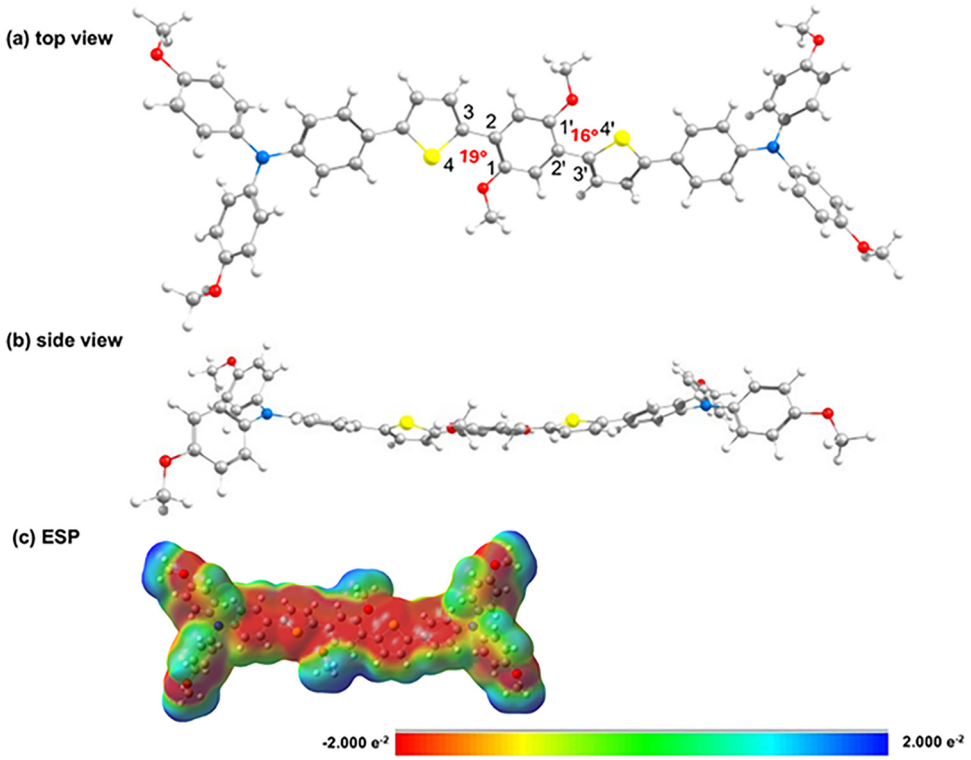

Fig. 3 (a) Top view of the optimized geometry of **NS-1** as obtained at the CAM-B3LYP/cc-PVTZ level of theory and the dihedral angle (degree) between oxy-benzene and thiophene units are shown, (b) side view of the optimized geometry of **NS-1** as obtained at the CAM-B3LYP/cc-PVTZ level of theory, and the (c) electrostatic surface potential (ESP) map of **NS-1**: red and blue colors represent the electron-rich and electron-poor regions, respectively.

the presence of the perovskite layer, with Spiro-OMeTAD included as a reference. The investigation began with the assessment of charge-carrier mobility. To examine the intrinsic charge transport capabilities of **NS-1** and **NS-2**, the space-charge-limited current (SCLC) method was employed. Hole-only devices were fabricated using the architecture ITO/PEDOT:PSS/**NS-1** or **NS-2**/Ag. The complete fabrication methodology is provided in Section 6 of the SI. The SCLC measurements were analysed by fitting the modified Mott–Gurney equation (eqn (1))[39,40] to the measured *J*–*V* curve, as shown in Fig. 5. The corresponding device architectures are depicted in the insets of Fig. 5.

$$J = \frac{9}{8}\mu\varepsilon_r\varepsilon_o\frac{V^2}{d^3}\exp\left(0.891\gamma\sqrt{\frac{V}{d}}\right) \quad (1)$$

where μ is the charge carrier mobility, ε_0 is the vacuum permittivity, J is the current density (area $\sim$ 6.6 mm^2), ε_r is the relative permittivity of the material ($\sim$3.4), d is the thickness of **NS-1** or **NS-2** (100 nm), γ symbolizes the empirical fitting parameter that characterizes the extent of the electric field dependence of charge carrier mobility and V is the applied voltage.

The hole mobility extracted values for **NS-1** and **NS-2** were found to be 1.31×10^{-3} cm^2 V^{-1} s^{-1} and 1.51×10^{-3} cm^2 V^{-1} s^{-1}, respectively (Table S11 presents the average values obtained from five devices). These values are comparable in magnitude to the hole mobility of Spiro-OMeTAD, which ranges from 10^{-4} to 10^{-3} cm^2 V^{-1} s^{-1}.[41,42] This confirms that both **NS-1** and **NS-2** are strongly p-type, will favour hole transport in PSCs.

2.6. Structural and optical characterization

Further, the conventional n–i–p device structure of the PSCs and the corresponding energy level alignment of the newly developed HTMs, **NS-1** and **NS-2**, are shown in Fig. 6(a) and (b), respectively. The HOMO energy levels of **NS-1** (−4.9 eV) and **NS-2** (−5.1 eV) are comparable to that of Spiro-OMeTAD (−5.2 eV), enabling effective hole extraction from the perovskite absorber layer ($Cs_{0.05}(FA_{0.79}MA_{0.16})_{0.95}Pb(I_{0.77}Br_{0.23})_3$), which typically exhibits a valence band maximum around −5.6 eV.[43,44] Additionally, the LUMO energy levels of the alternative materials nearly match those of Spiro-OMeTAD values, effectively preventing undesired electron transfer at the perovskite/**NS-1** or **NS-2** interface maintaining charge selectivity.[42,45] The HOMO level of Spiro-OMeTAD was adopted from literature reports determined by CV and UPS under comparable electrochemical conditions and is used here as a reference benchmark.[41,46] Overall, both HTM materials of this work, demonstrate excellent energy level alignments in the n–i–p architecture of PSCs, confirming their potential as viable replacements in PSCs. However, **NS-1** was not further pursued for optimized device fabrication due to its inferior photovoltaic performance relative to **NS-2**, as detailed in SI Section 13. In contrast, the combination of high hole mobility and excellent processability in chlorobenzene renders **NS-2** a more suitable

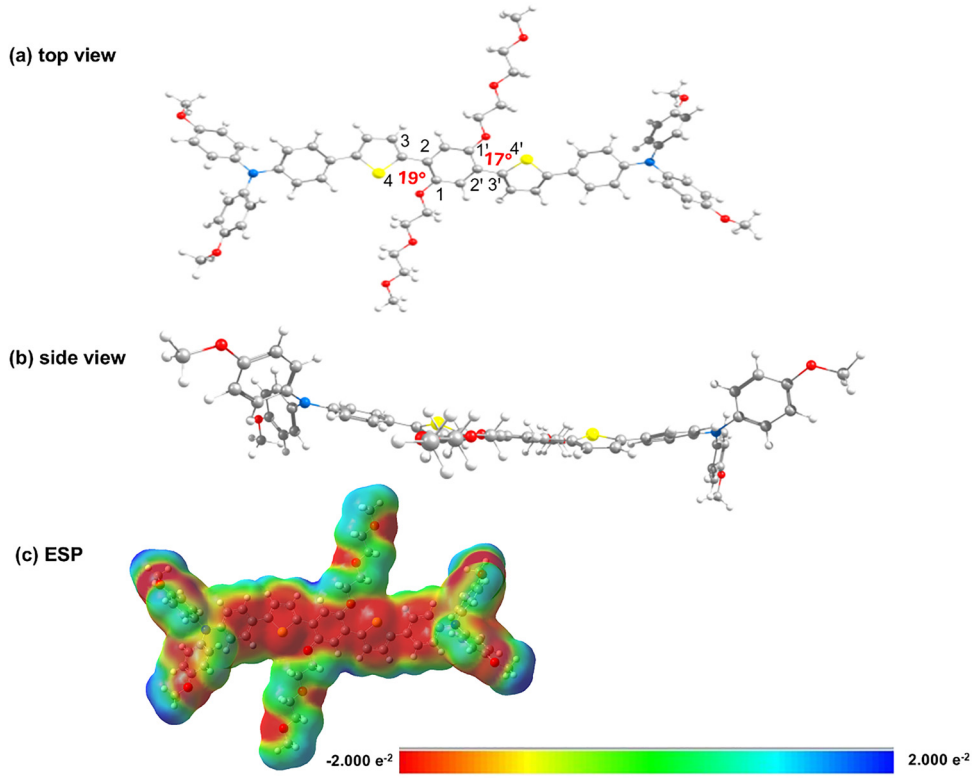

Fig. 4 (a) Top view of the optimized geometry of **NS-2** as obtained at the CAM-B3LYP/cc-PVTZ level of theory and the dihedral angle (degree) between oxy-benzene and thiophene units are shown, (b) side view of the optimized geometry of **NS-2** as obtained at the CAM-B3LYP/cc-PVTZ level of theory, and the (c) electrostatic surface potential (ESP) maps of **NS-2**: red and blue colors represent the electron-rich and electron-poor regions, respectively.

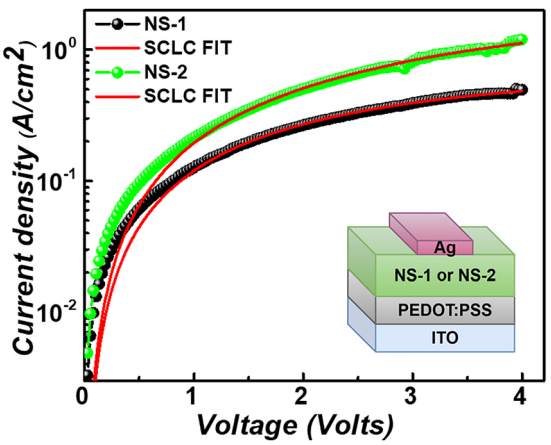

Fig. 5 The semi-logarithmic *J*–*V* characteristics were analysed using the modified Mott–Gurney SCLC equation to determine the hole mobilities of the **NS-1** and **NS-2** compounds.

and reliable hole-transporting material for perovskite solar cells.

Furthermore, UV-vis and XRD characterizations were conducted to verify that the presence of **NS-2** does not adversely affect the buried perovskite layer. As shown in Fig. 6(c), **NS-2** exhibits an absorption profile comparable to that of Spiro-OMeTAD. This suggests that the **NS-2** layer does not introduce additional parasitic absorption and therefore does not impede light transmission to the perovskite absorber, similar to the conventional Spiro-OMeTAD HTM. Since, the optical behaviour of **NS-2** closely matches that of Spiro-OMeTAD, it highlights its potential as an effective HTM.[47,48] Moreover, to investigate the structural integrity of the perovskite/**NS-2** interface layer, XRD analysis was also performed. Fig. 6(d) depicts the XRD patterns of the bare perovskite, perovskite/Spiro-OMeTAD, and perovskite/**NS-2** films in the 2 theta range. The bare perovskite film exhibits an FWHM of 0.188, while the perovskite/Spiro-OMeTAD sample shows an almost similar FWHM of 0.182.

In contrast, the perovskite/**NS-2** film demonstrates the narrowest FWHM of 0.171. This result indicates that **NS-2** forms a better interfacial contact with the perovskite layer (the raw data of these three films are depicted in Fig. S7). The XRD patterns show no emergence of new diffraction peaks or noticeable peak shifts compared to the bare perovskite film, confirming that the intrinsic crystal structure of the perovskite remains unaltered. This indicates that **NS-2** does not penetrate into or disrupt the bulk perovskite layer. Instead, **NS-2** passivates interfacial defects at the perovskite/HTM interface, in contrast to Spiro-OMeTAD.[49,50] Additionally, the XRD patterns show a weak Pb^{2+} peak at $\sim 12^{\circ}$ in the perovskite/Spiro-OMeTAD sample, whereas this peak is reduced in the perovskite/**NS-2** sample, indicating more effective passivation of undercoordinated Pb^{2+} sites. The suppression of the Pb^{2+} peak in **NS-2** can be attributed to the

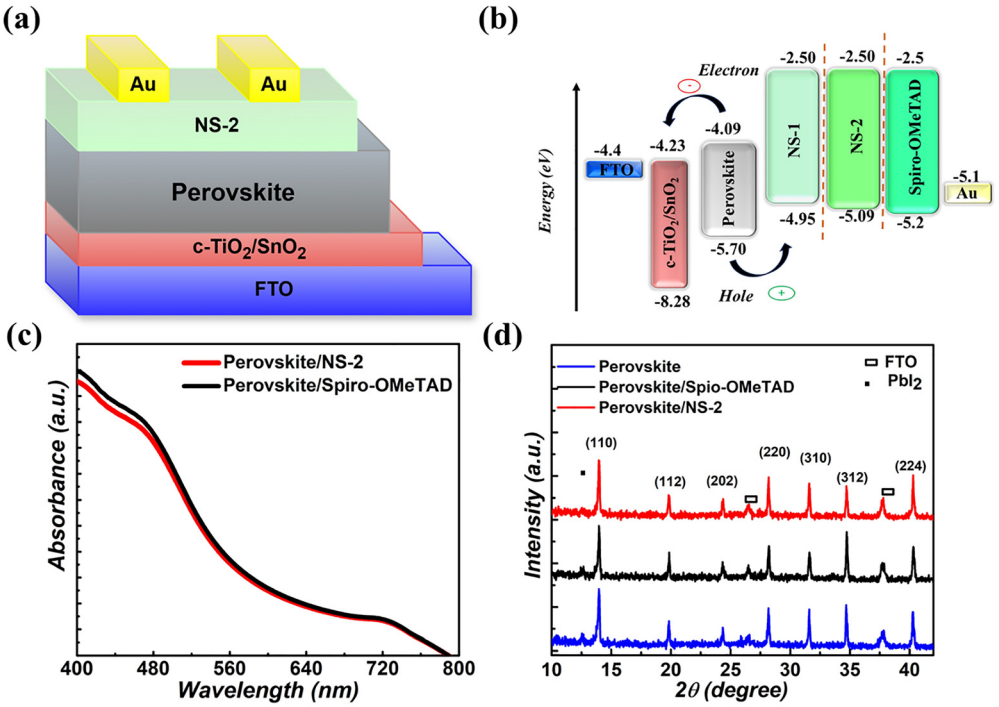

Fig. 6 (a) Device architecture schematic of the PSC, (b) energy level positioning of the perovskite layer with Spiro-OMeTAD and the two alternative HTM materials, (c) UV-vis of the perovskite absorbers fabricated with Spiro-OMeTAD and **NS-2** as the HTMs and (d) XRD patterns of bare perovskite, Spiro-OMeTAD, and **NS-2** deposited on perovskite films.

Lewis base character of the HTM, which facilitates coordination with undercoordinated Pb^{2+} ions at the perovskite interface, leading to interface passivation and stability.[50–53] Thus, both XRD and UV-vis analyses confirm that **NS-2**, as an HTM, does not adversely affect the perovskite layer, and instead acts as an efficient interfacial passivation layer. Since the HTM is deposited after complete perovskite crystallization, its role is confined to interfacial modification rather than bulk structural alteration.[54]

2.7. Scanning electron microscopy

To evaluate the surface morphology and uniformity of the perovskite/Spiro-OMeTAD and perovskite/**NS-2** samples, field emission scanning electron microscopy (FE-SEM) analysis was performed. Fig. 7(a) and (b) show the perovskite/Spiro-OMeTAD and perovskite/**NS-2** films, respectively. The images reveal that the Spiro-OMeTAD layer is relatively thicker than the **NS-2** layer, which may lead to increased charge accumulation in the Spiro-OMeTAD device.[55,56] Similar images have been previously reported in the literature.[55] Moreover, profilometer measurements (Fig. S12) corroborate the FE-SEM observations, indicating a thickness of ~180 nm for the Spiro-OMeTAD film and ~120 nm for **NS-2**. To investigate whether variations in the HTM thickness between Spiro-OMeTAD and **NS-2** affect device structure, cross-sectional images of PSCs were acquired. Fig. S8(a) and (b) show devices employing Spiro-OMeTAD and **NS-2** as the HTMs, respectively. The images clearly reveal a difference in the HTM thickness, with **NS-2** forming a thinner layer than Spiro-OMeTAD. Importantly, the deposition of **NS-2** does not influence perovskite growth and preserves the overall device integrity, consistent with the morphology observed in Spiro-OMeTAD-based devices.[26,57] These results indicate that **NS-2** can effectively replace Spiro-OMeTAD as the HTM without compromising the device structure.

2.8. Charge transfer dynamics

Additionally, steady-state PL and time-resolved photoluminescence (TRPL) measurements were carried out to further study the interfacial charge extraction between perovskite and **NS-2** as well as Spiro-OMeTAD. Fig. 7(c) shows the PL spectra of the bare perovskite, perovskite/Spiro-OMeTAD and perovskite/**NS-2** films. This comparison allows for evaluating the influence of Spiro-OMeTAD and **NS-2** on the charge extraction efficiency from the absorber. Compared to the bare perovskite film, both the Perovskite/Spiro-OMeTAD and Perovskite/**NS-2** configurations exhibit significant PL quenching, indicating that the HTMs effectively extract photogenerated holes. Notably, the Perovskite/**NS-2** device shows a relatively higher quenching effect than the Spiro-OMeTAD device, which suggests that **NS-2** results in the efficient extraction of carriers before recombination occurs.[55,58,59]

To validate steady-state PL observations, TRPL studies were further performed. The TRPL decay transients of Fig. 7(d), analysed using the double exponential decay model, as described by eqn (2) and τ_{avg} denoting average carrier lifetime,

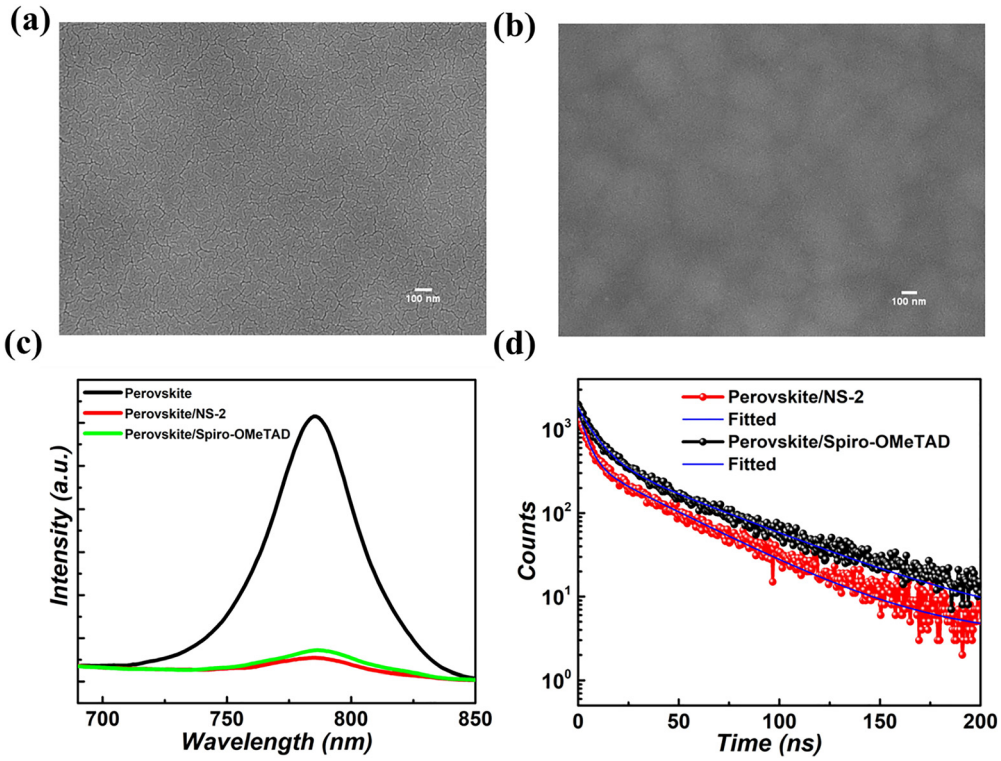

Fig. 7 (a) FE-SEM image of the perovskite/Spiro-OMeTAD and (b) FE-SEM image of the perovskite/**NS-2**. (c) Steady-state photoluminescence (PL) spectra and (d) time-resolved photoluminescence (TRPL) decay profiles of the perovskite films with Spiro-OMeTAD and **NS-2** as HTMs.

was calculated as described in eqn (3).[60]

$$I(t) = I_O + A_1 \exp^{\frac{-t}{\tau_1}} + A_2 \exp^{\frac{-t}{\tau_2}} \quad (2)$$

$$\tau_{avg} = (A_1{\tau_1}^2 + A_2{\tau_2}^2)/(A_1\tau_1 + A_2\tau_2) \quad (3)$$

where τ_1 and τ_2 correspond to the fast and slower decay components, respectively, and t is the time variable. The amplitudes A_1 and A_2 correspond to the relative contributions of these decay processes.

The perovskite/**NS-2** exhibits a shorterτ_{avg} = 27.25 ns, suggesting a faster charge (hole) transfer process at the Perovskite/**NS-2** interface. In contrast, the longer τ_{avg} = 33.53 ns for perovskite/Spiro-OMeTAD indicates relatively slower hole extraction. The detailed carrier lifetime data are summarized in Table S12. Overall results validate that **NS-2** enhances charge transfer at the perovskite/Spiro-OMeTAD interface, and these results validate that **NS-2** not only facilitates enhanced charge mobility but also improves defect passivation at the interface.[56,60,61]

To further understand the passivation effect of **NS-2** and its impact on charge carrier dynamics, space-charge limited current measurements were carried out, which determined the hole mobility and defect density by fabricating hole-only devices configured as ITO/PTAA/Perovskite/Spiro-OMeTAD/Au and ITO/PTAA/Perovskite/**NS-2**/Au, as illustrated in Fig. S10. The experimental methodology is detailed in SI Section 10. Fig. S11 depicts the *J*–*V* curves that were fitted to the modified Mott–Gurney equation (eqn (1)) to extract hole mobility.[32,62] The hole mobility of the device with the **NS-2** HTM was found to be 2.88 × 10^{-3} cm^2 V^{-1} s^{-1}, indicating significantly higher mobility compared to that of Spiro-OMeTAD (1.74 × 10^{-3} cm^2 V^{-1} s^{-1}).[26,63] The slightly enhanced hole mobility observed for the **NS-2** device is primarily attributed to the presence of ether-based side chains. Importantly, the introduction of ether side chains does not alter the conjugated backbone but improves charge transport indirectly by reducing energetic disorder, and improving interfacial hole extraction. The polar ether functionalities introduce the Lewis-base character, which facilitates favourable interfacial interactions with the perovskite layer, leading to a reduced trap density and lower interfacial resistance. In addition, the flexible ether side chains can promote more homogeneous molecular organization, which is known to support efficient charge hopping in small-molecule and polymeric organic semiconductors.[64–67]

The trap density determined using the *J*–*V* characteristics (log–log plot) are presented in Fig. 8(a), where Spiro-OMeTAD and **NS-2** were employed as hole-transporting materials, based on the analysis using eqn (4).[68]

$$\eta_{trap} = \frac{2V_{TFL}\varepsilon_r\varepsilon_o}{qd^2} \quad (4)$$

Here, η_{trap} is the trap density, V_{TFL} denotes the trap-filled limited voltage, d symbolizes the thickness of the active region (~500 nm), q represents the fundamental charge, η_{trap} is the

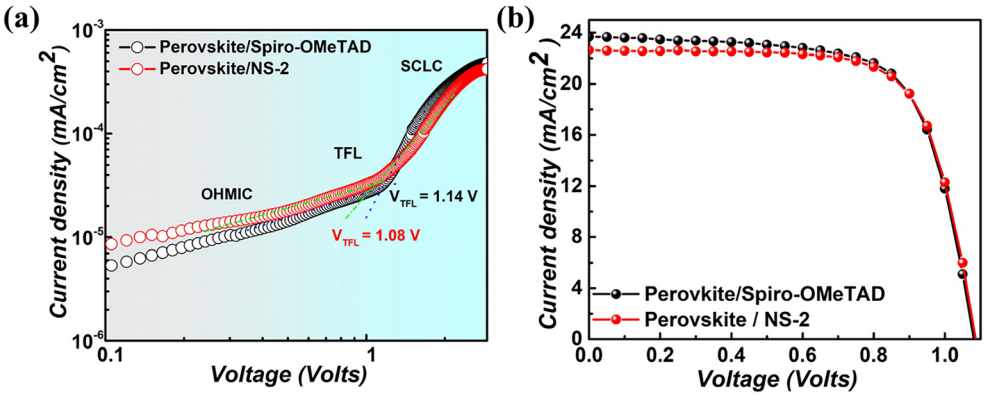

Fig. 8 Performance comparison of perovskite solar cells employing Spiro-OMeTAD and **NS-2** as HTMs. (a) Trap density analysis derived from space-charge-limited current measurements and (b) current density–voltage characteristics of the corresponding devices measured under standard illumination conditions.

defect density, ε_r ($\sim$44)[69] denotes the material relative dielectric constant and ε_o is the permittivity of free space.

The trap density of the **NS-2**-based device was estimated to be 2.10 $\times$ 10^{16} cm^{-3}, whereas for Spiro-OMeTAD, the HTM device showed a slightly higher value 2.22 $\times$ 10^{16} cm^{-3}. The reduced trap density in the perovskite/**NS-2** configuration suggests better interfacial contact and more effective defect passivation compared to the perovskite/Spiro-OMeTAD interface. This enhanced passivation suppresses non-radiative recombination pathways and promotes more efficient charge extraction and transport, which can reduce energy losses and support more stable device operation.[70,71] Therefore, it can be concluded that **NS-2** effectively mitigates the degradation of the device.

2.9. Photovoltaic performance

After completing the preliminary investigations for the suitability of **NS-2** and Spiro-OMeTAD, electrical parameters such as the open-circuit voltage (V_{OC}), fill factor (FF) and short-circuit current (J_{SC}) of the PSCs were acquired by a *J–V* plot under AM 1.5G illumination (100 mW cm^{-2}, AM-1.5G). The devices were fabricated as described in SI section 11. Initial tests were performed using undoped **NS-1** and **NS-2** as HTMs, as shown in Fig. S13, with an average of 5 PSC parameters summarized in Table S13. The corresponding devices exhibited a low PCE of approximately $\sim$2% for **NS-1** and $\sim$6% for **NS-2**. Due to this limited performance, both materials were subsequently doped using conditions similar to those employed for Spiro-OMeTAD. Even after doping, **NS-1**-based devices delivered a modest PCE of 4.19%, which can be attributed to poor solubility in chlorobenzene and non-uniform film formation. In contrast, incorporation of doped **NS-2** resulted in significantly improved efficiencies. The corresponding *J–V* characteristics are presented in Fig. S14, while the photovoltaic parameters for five individual devices are summarized in Table S14. Based on these findings, further optimization was carried out using **NS-2**. Concentration-dependent studies in CB were performed at 10, 20, 60, and 90 mg mL^{-1}, with the corresponding photovoltaic performances shown in Fig. S15 and Table S15 summarizing the performance of the best five devices at each concentration, with 20 mg mL^{-1} yielding the highest efficiency, since a balanced concentration provides the best film quality.[26] Additionally, the spin-coating speed was then optimized, and the *J–V* characteristics of the devices are shown in Fig. S16 and the photovoltaic performance metrics are summarized in Table S16, which implies that 3000 rpm was identified as optimal. Precise control of the spin-coating speed is crucial, as it directly influences film surface coverage, thickness and morphology, which in turn affect charge transport.[72] Following these optimizations, devices prepared with **NS-2** at 20 mg mL^{-1} and 3000 rpm were compared with reference devices employing Spiro-OMeTAD. The corresponding *J–V* characteristics are shown in Fig. 8(b). The photovoltaic parameters calculated over 15 individual cells using Spiro-OMeTAD and **NS-2** as the HTMs are summarized in Table 2.

On average, the **NS-2**-based PSCs exhibit a J_{SC} of 22.51 $\pm$ 0.09 mA cm^{-2}, a V_{OC} of 1.08 $\pm$ 0.01 V, and an FF of 0.70 $\pm$ 0.01, resulting in an average PCE of 17.16 $\pm$ 0.22%. In comparison, the Spiro-OMeTAD-based devices deliver an average PCE of 17.31 $\pm$ 0.30%, with a J_{SC} of 23.29 $\pm$ 0.34 mA cm^{-2} and a V_{OC} of 1.08 $\pm$ 0.01 V, while the fill factor remains comparable at 0.69 $\pm$ 0.01. The average performance data for the **NS-2**-based devices demonstrate excellent reproducibility, indicating reliable processing and stable material behaviour under identical fabrication conditions. Moreover, the narrower standard deviation in the **NS-2**-based device results clearly shows that the devices maintain highly consistent performance metrics across multiple batches. The statistical distribution of the photovoltaic parameters is visualized in Fig. 9, while the histogram (Fig. S17) shows the tight clustering of values for device performance parameters. This narrow distribution further confirms the stability of the **NS-2** layer during processing and measurement, highlighting its ability to produce homogeneous films that enable stable interfacial contact between the perovskite absorber and top electrode. Moreover, both the average and champion power conversion efficiencies confirm that devices employing the newly designed **NS-2** HTM exhibit performance comparable to those based on Spiro-OMeTAD. The

Table 2 The average photovoltaic parameters for 15 best devices fabricated with **NS-2** and Spiro-OMeTAD; performance parameters for the champion device are shown in parentheses

HTMs	J_{SC} (mA cm^{-2})	V_{OC} (V)	FF (%)	PCE (%)
Spiro-OMeTAD	23.29 ± 0.34 (23.69)	1.08 ± 0.01 (1.08)	0.69 ± 0.01 (0.70)	17.31 ± 0.30 (17.69)
NS-2	22.51 ± 0.09 (22.63)	1.08 ± 0.01 (1.09)	0.70 ± 0.01 (0.71)	17.16 ± 0.22 (17.50)

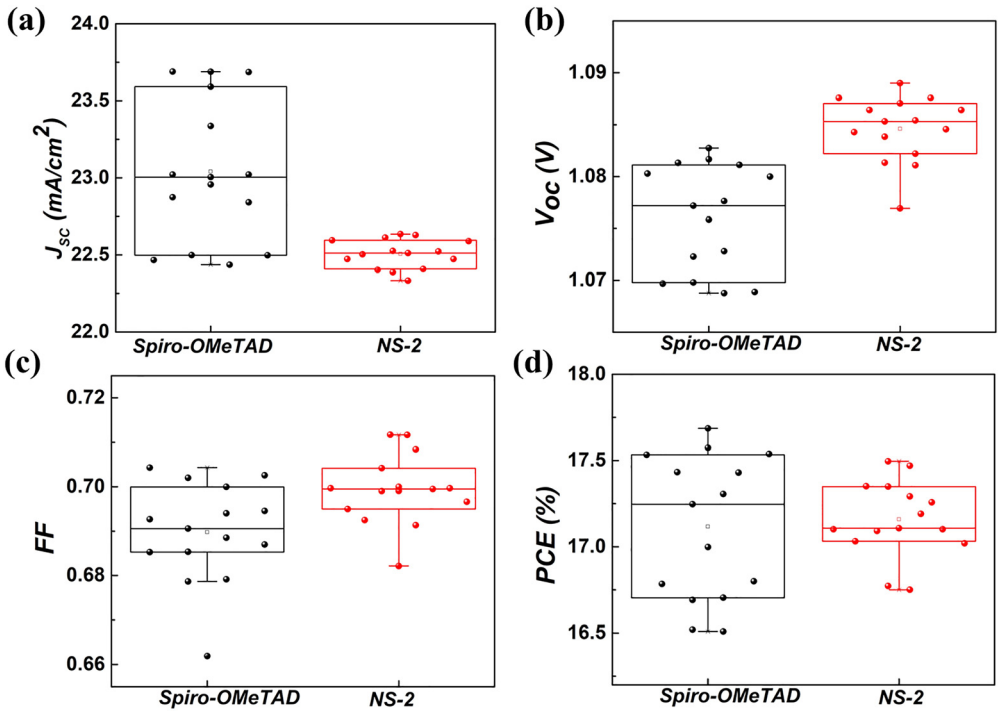

Fig. 9 Statistical distribution of the photovoltaic parameters for PSCs using Spiro-OMeTAD and **NS-2** as HTMs: (a) short-circuit current density, (b) open-circuit voltage, (c) fill factor (FF) and (d) power conversion efficiency.

champion **NS-2** device shows a marginally higher V_{OC} (~0.9%) and fill factor (~1.4%) relative to Spiro-OMeTAD. The enhanced V_{OC} is attributed to more efficient charge extraction, as evidenced by PL and TRPL analyses, while the improved FF arises from reduced trap density and suppressed non-radiative recombination, as confirmed by SCLC measurements.[73] Collectively, these results demonstrate that **NS-2** enables efficient charge transport and effective passivation at the perovskite/HTM interface. Importantly, this study demonstrates **NS-2** as a low-cost, stable alternative HTM capable of delivering performance comparable to the state-of-the-art Spiro-OMeTAD, highlighting the novelty and practical relevance of the proposed design.[71,74]

To further validate these observations, the hysteresis index (HI) for the devices with Spiro-OMeTAD and **NS-2** was calculated using well-known eqn (5).[75]

$$\text{Hysteresis index} = \frac{\text{PCE}_{\text{reverse}} - \text{PCE}_{\text{forward}}}{\text{PCE}_{\text{reverse}}} \quad (5)$$

Eqn (5) explains the extent of current-density curve distortion under forward and reverse scan directions. Fig. 10(a) depicts the *J–V* plot for the Spiro-OMeTAD device, while Fig. 10(b) presents the corresponding plot for the **NS-2** PSC, both measured under forward and reverse bias sweeps. A pronounced difference in hysteresis behaviour was observed: the **NS-2** device exhibited a much lower HI value of 0.17% compared to the Spiro-OMeTAD-based device (0.68%). The decreased hysteresis in **NS-2** devices is mainly due to better interfacial contact, which effectively suppresses charge accumulation at the interface, leading to more stable device operation. Table S17 provides the calculated values for both scanning directions, from which the HI was extracted, further validating our observation. Thus, the lower hysteresis indicates higher operational stability for **NS-2** based devices, making them more promising for reliable and reproducible PSCs.[76]

Additionally, to determine the effect of various device resistances in the n–i–p architecture of the PSCs, dark *J–V* analysis was performed, as shown in Fig. 10(c), for both **NS-2** and Spiro-OMeTAD-based devices. It is observed that the **NS-2**-based device demonstrates a relatively lower leakage current and series resistance (R_s), along with a higher shunt resistance (R_{sh}) compared to the Spiro-OMeTAD-based device. Specifically, from Table S18, the average R_s and R_{sh} of the 15 devices for the **NS-2** devices are 62.07 Ω and 11 850.54 Ω, respectively. In

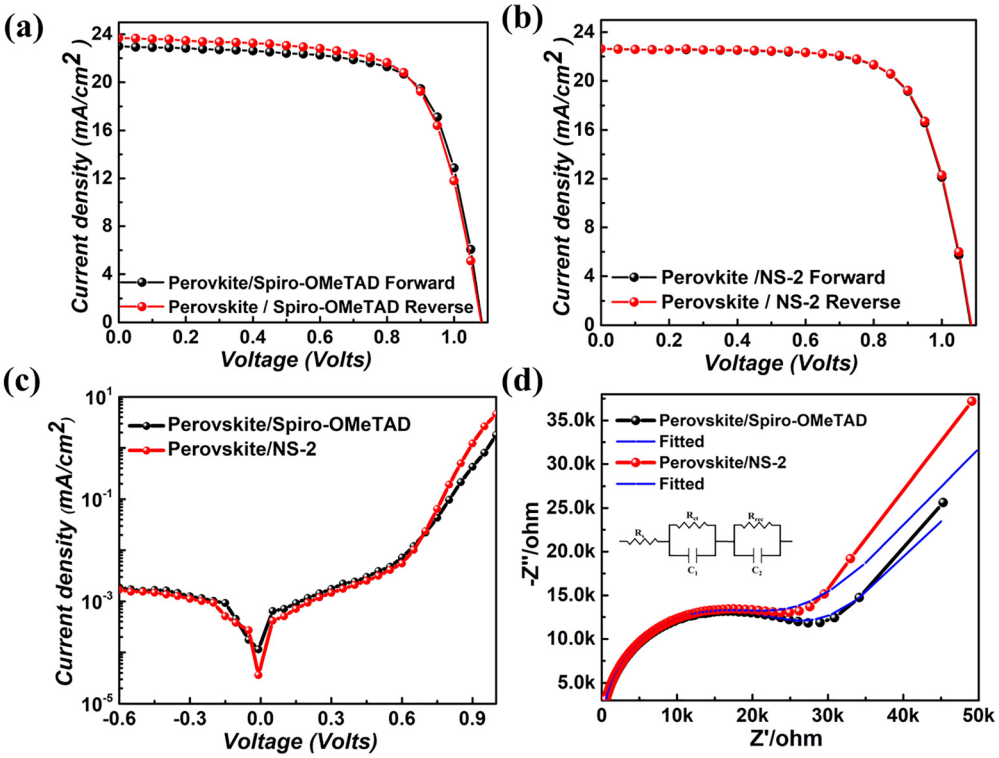

Fig. 10 *J–V* hysteresis behaviour of the devices based on (a) Spiro-OMeTAD and (b) **NS-2** HTMs measured under standard illumination conditions. (c) Dark current density–voltage characteristics and (d) Nyquist plots obtained from electrochemical impedance spectroscopy (EIS) measurement for both the devices.

contrast, the Spiro-OMeTAD-based devices exhibit a slightly higher average R_s of 66.17 Ω and a lower average R_{sh} of 10 708.55 Ω. These results indicate that **NS-2** facilitates reduced resistive losses and better charge extraction pathways, which suppress recombination and leakage currents. The higher shunt resistance further reflects better interfacial contact between the perovskite layer and the HTM. Together, these factors mitigate interfacial degradation and can contribute to the enhanced operational stability of **NS-2**-based devices.[77,78]

To further describe the impact of **NS-2** on the interfacial electrical characteristics, EIS was performed. The Nyquist plots presented in Fig. 10(d) are interpreted using the equivalent circuit model illustrated in the inset. The circuit parameters (R_s), recombination resistance (R_{rec}) and charge transfer resistance (R_{ct}) were extracted by fitting the impedance data, with the values summarised in Table S19. The **NS-2**-based PSCs demonstrated a lower series resistance of 123.5 Ω cm^2 and an R_{ct} of 65.86 Ω cm^2, in comparison with the Spiro-OMeTAD device, which exhibited an R_s of 150.7 Ω cm^2 and an R_{ct} of 5429 Ω cm^2. This indicates that the **NS-2**-based PSCs suggest improved charge transport, more efficient charge extraction, and better contact at the interfaces, as compared to the Spiro-OMeTAD-based device. Moreover, the R_{rec} was significantly higher for the **NS-2** device (21050 Ω cm^2) than for the Spiro-OMeTAD device (18 775 Ω cm^2), which reduces carrier loss as a form of heat. These observations confirm that **NS-2** leads to improved charge transport dynamics and interface stability, as supported by dark *J–V* measurements.[45]

To further assess the reliability of the photovoltaic parameters, external quantum efficiency (EQE) measurements were performed, and the corresponding spectra are shown in Fig. 11(a). The **NS-2**-based devices exhibit a slightly lower EQE (~80%) compared to Spiro-OMeTAD-based devices (~83%) at 600 nm, consistent with the marginally lower J_{SC} observed in *J–V* measurements. The integrated current densities derived from the EQE spectrum are 22.42 mA cm^{-2} for the **NS-2** device and 22.51 mA cm^{-2} for the Spiro-OMeTAD device, which closely match the current density values obtained from the *J–V* characterization, confirming the accuracy and reliability of the measured photovoltaic performance.[37,79,80]

2.10. Stability

To further verify the operational stability under continuous working conditions, maximum power point (MPP) tracking was conducted, as shown in Fig. 11(b). The **NS-2**-based devices maintain a nearly constant power conversion efficiency of ~17% during MPP tracking, indicating a stable power output over time. In contrast, devices employing Spiro-OMeTAD exhibit a gradual decline in efficiency under identical conditions. Notably, a crossover in the MPP tracking curves is observed at early operation times, where Spiro-OMeTAD-based devices display a slightly higher initial PCE, followed by a more pronounced performance decay. In comparison, **NS-2**-based devices exhibit minimal transient behaviour and superior performance retention, thereby demonstrating improved operational stability under realistic working conditions.[55,81]

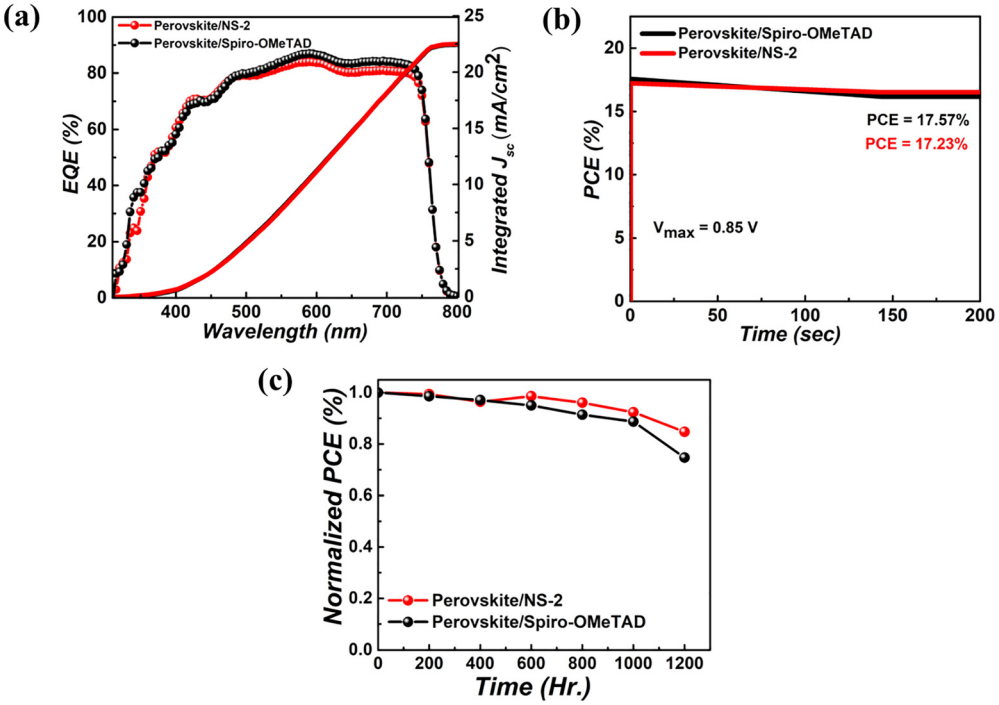

Fig. 11 Perovskite solar cells employing **NS-2** and Spiro-OMeTAD as HTMs: (a) EQE spectra and (b) maximum power point (MPP) tracking of the corresponding devices and (c) operational stability of both devices measured over time.

Moreover, to validate observations that **NS-2** can outperform Spiro-OMeTAD in terms of device stability, stability tests were also conducted for both HTMs, and the comparative performance of the **NS-2** and Spiro-OMeTAD champion devices is shown in Fig. 11(c). The **NS-2**-based devices retained approximately 84% of the initial PCE after 1200 hours aging under ambient conditions (26 °C, relative humidity of 35 ± 5%) without encapsulation, whereas Spiro-OMeTAD-based devices retained only about ~73%. A minor fluctuation in the normalized PCE is observed for the **NS-2**-based device between 400 and 600 hours. This variation lies within experimental scatter, and is attributed to gradual interfacial stabilization during aging rather than to a true performance enhancement, consistent with previously reported behaviour in perovskite solar cells.[80,82–84] The stability measurements were performed periodically. This significant increase in device stability indicates that the **NS-2**-based device shows superior operational stability over Spiro-OMeTAD. Furthermore, contact angle measurements using water were conducted to evaluate the moisture resistance of the HTMs and to gain deeper insight into the enhanced stability of **NS-2**-based PSCs. Measurements were taken at three different positions on each sample to account for local variations and ensure statistical reliability. The corresponding data are presented in Fig. S19 for Spiro-OMeTAD and Fig. S20 for **NS-2**. Table S20 summarizes the contact angles of perovskite films with the two HTMs, showing average values of ~91° and ~73° for **NS-2** and Spiro-OMeTAD, respectively. The champion **NS-2** sample exhibited a contact angle of 95.2°, compared to 74.5° for Spiro-OMeTAD. It should be noted that water contact angle measurements probe the exposed HTM surface of the perovskite/HTM stack and therefore reflect changes in the overall surface energy and moisture resistance rather than the direct measurement of buried interfacial coordination.[85,86] The results confirm that **NS-2** enhances resistance to moisture ingress and improve long-term device stability. Overall, these results indicate that the newly designed **NS-2** HTM effectively addresses the stability limitations of conventional Spiro-OMeTAD-based devices while maintaining competitive photovoltaic performance.

3. Conclusions

In summary, we have designed and synthesized two novel hole-transporting materials (HTMs), **NS-1** and **NS-2**, based on a thiophene–benzene–thiophene (TBT) central core and triarylamine peripheral groups. The key difference between the two lies in their side chains: **NS-1** contains methoxy (–OCH_3) substituents, while **NS-2** incorporates polar ethylene glycol side chains. These newly developed HTMs are more cost-effective than the widely used Spiro-OMeTAD and exhibit favourable optical and electrochemical properties, including suitable HOMO–LUMO energy levels, high conductivity and efficient hole mobility. Compared to **NS-1**, **NS-2** shows a relatively deeper HOMO energy level and forms smoother, more uniform films. As a result of its better energy level alignment and enhanced charge transport properties, the perovskite solar cell fabricated with **NS-2** achieved a maximum PCE of 17.50%, significantly higher than that of the **NS-1**-based device (4.96%) and approaching the performance of the reference device with

Spiro-OMeTAD (17.69%). Furthermore, the **NS-2**-based device demonstrated excellent operational stability, maintaining approximately 84% of its initial efficiency after over 1200 hours. These findings confirm that **NS-2** delivers photovoltaic performance nearly equivalent to Spiro-OMeTAD while offering superior stability and substantially lower material cost, thereby addressing two of the major critical challenges associated with conventional HTMs and advancing the prospects for scalable, cost-effective perovskite solar cell technology.

Conflicts of interest

There are no conflicts to declare.

Data availability

The data supporting the findings of this study are available within the article, its supplementary information (SI) and also from the corresponding author upon reasonable request. Supplementary information: synthesis details of **NS-1** and **NS-2**, cost analysis, NMR spectra, CV curves, TGA, DSC, computational methodology, SCLC, XRD, FESEM, TRPL, perovskite solar cell fabrication, profilometer measurements, *J–V* characterization, hysteresis index, EIS and contact angle measurements. See DOI: **https://doi.org/10.1039/d5qm00763a**.

Acknowledgements

KNS acknowledges financial support from SRM University-AP through a seed grant (SRMAP/URG/SEED/2023-24/028) and DST-FIST [SR-FST-CS-1-2021-219 (C)] for supporting the Department of Chemistry, SRM University-AP. UKP gratefully acknowledges financial support extended from the Science and Engineering Research Board (SERB) project CRG/2023/008061/EEC and from Shiv Nadar IoE. AS expresses sincere gratitude to Shiv Nadar IoE for research fellowships.

References

1 Best Research-Cell Efficiency Chart | Photovoltaic Research | NLR, **https://www.nrel.gov/pv/cell-efficiency**, (accessed 22 January 2026).
2 Y. Duan, Y. Chen, Y. Wu, Z. Liu, S. Liu and Q. Peng, A Comprehensive Review of Organic Hole-Transporting Materials for Highly Efficient and Stable Inverted Perovskite Solar Cells, *Adv. Funct. Mater.*, 2024, **34**, 2315604.
3 F. H. Isikgor, S. Zhumagali, L. V. T. Merino, M. De Bastiani, I. McCulloch and S. De Wolf, Molecular engineering of contact interfaces for high-performance perovskite solar cells, *Nat. Rev. Mater.*, 2023, **8**, 89–108.
4 J. Zhou, L. Tan, Y. Liu, H. Li, X. Liu, M. Li, S. Wang, Y. Zhang, C. Jiang, R. Hua, W. Tress, S. Meloni and C. Yi, Highly efficient and stable perovskite solar cells via a multifunctional hole transporting material, *Joule*, 2024, **8**, 1691–1706.
5 S. Liu, J. Li, W. Xiao, R. Chen, Z. Sun, Y. Zhang, X. Lei, S. Hu, M. Kober-Czerny, J. Wang, F. Ren, Q. Zhou, H. Raza, Y. Gao, Y. Ji, S. Li, H. Li, L. Qiu, W. Huang, Y. Zhao, B. Xu, Z. Liu, H. J. Snaith, N.-G. Park and W. Chen, Buried interface molecular hybrid for inverted perovskite solar cells, *Nature*, 2024, **632**, 536–542.
6 P. Murugan, T. Hu, X. Hu and Y. Chen, Advancements in organic small molecule hole-transporting materials for perovskite solar cells: past and future, *J. Mater. Chem. A*, 2022, **10**, 5044–5081.
7 A. F. Latypova, N. A. Emelianov, D. O. Balakirev, P. K. Sukhorukova, N. K. Kalinichenko, P. M. Kuznetsov, Y. N. Luponosov, S. M. Aldoshin, S. A. Ponomarenko, P. A. Troshin and L. A. Frolova, Design Principles for Organic Small Molecule Hole-Transport Materials for Perovskite Solar Cells: Film Morphology Matters, *ACS Appl. Energy Mater.*, 2022, **5**, 5395–5403.
8 F. Cai, J. Cai, L. Yang, W. Li, R. S. Gurney, H. Yi, A. Iraqi, D. Liu and T. Wang, Molecular engineering of conjugated polymers for efficient hole transport and defect passivation in perovskite solar cells, *Nano Energy*, 2018, **45**, 28–36.
9 Z. Yu and L. Sun, Inorganic Hole-Transporting Materials for Perovskite Solar Cells, *Small Methods*, 2018, **2**, 1700280.
10 J. Burschka, A. Dualeh, F. Kessler, E. Baranoff, N.-L. Cevey-Ha, C. Yi, M. K. Nazeeruddin and M. Grätzel, Tris(2-(1H-pyrazol-1-yl)pyridine)cobalt(III) as p-Type Dopant for Organic Semiconductors and Its Application in Highly Efficient Solid-State Dye-Sensitized Solar Cells, *J. Am. Chem. Soc.*, 2011, **133**, 18042–18045.
11 G. Ren, W. Han, Y. Deng, W. Wu, Z. Li, J. Guo, H. Bao, C. Liu and W. Guo, Strategies of modifying spiro-OMeTAD materials for perovskite solar cells: a review, *J. Mater. Chem. A*, 2021, **9**, 4589–4625.
12 S. Wang, Z. Huang, X. Wang, Y. Li, M. Günther, S. Valenzuela, P. Parikh, A. Cabreros, W. Xiong and Y. S. Meng, Unveiling the Role of tBP–LiTFSI Complexes in Perovskite Solar Cells, *J. Am. Chem. Soc.*, 2018, **140**, 16720–16730.
13 T. H. Schloemer, J. A. Christians, J. M. Luther and A. Sellinger, Doping strategies for small molecule organic hole-transport materials: impacts on perovskite solar cell performance and stability, *Chem. Sci.*, 2019, **10**, 1904–1935.
14 Y. Zhao, W. Zhou, Z. Han, D. Yu and Q. Zhao, Effects of ion migration and improvement strategies for the operational stability of perovskite solar cells, *Phys. Chem. Chem. Phys.*, 2021, **23**, 94–106.
15 L. Calió, S. Kazim, M. Grätzel and S. Ahmad, Hole-Transport Materials for Perovskite Solar Cells, *Angew. Chem., Int. Ed.*, 2016, **55**, 14522–14545.
16 T. Lei, J.-Y. Wang and J. Pei, Roles of Flexible Chains in Organic Semiconducting Materials, *Chem. Mater.*, 2014, **26**, 594–603.
17 S.-F. Yang, Z.-T. Liu, Z.-X. Cai, M. J. Dyson, N. Stingelin, W. Chen, H.-J. Ju, G.-X. Zhang and D.-Q. Zhang, Diketopyrrolopyrrole-Based Conjugated Polymer Entailing Triethylene Glycols as Side Chains with High Thin-Film Charge Mobility without Post-Treatments, *Adv. Sci.*, 2017, **4**, 1700048.

18 J. Mei and Z. Bao, Side Chain Engineering in Solution-Processable Conjugated Polymers, *Chem. Mater.*, 2014, **26**, 604–615.
19 J. Mei, D. H. Kim, A. L. Ayzner, M. F. Toney and Z. Bao, Siloxane-Terminated Solubilizing Side Chains: Bringing Conjugated Polymer Backbones Closer and Boosting Hole Mobilities in Thin-Film Transistors, *J. Am. Chem. Soc.*, 2011, **133**, 20130–20133.
20 N. Kamatham, O. A. Ibraikulov, P. Durand, J. Wang, O. Boyron, B. Heinrich, T. Heiser, P. Lévêque, N. Leclerc and S. Méry, On the Impact of Linear Siloxanated Side Chains on the Molecular Self-Assembling and Charge Transport Properties of Conjugated Polymers, *Adv. Funct. Mater.*, 2021, **31**, 2007734.
21 B. Kang, R. Kim, S. B. Lee, S.-K. Kwon, Y.-H. Kim and K. Cho, Side-Chain-Induced Rigid Backbone Organization of Polymer Semiconductors through Semifluoroalkyl Side Chains, *J. Am. Chem. Soc.*, 2016, **138**, 3679–3686.
22 K. Miao, G. J. Chae, X. Wu, Q. Shu, X. Zhu, B. Sun, J. Fan and S. Cho, Diketopyrrolopyrrole-based polymer with a semi-fluorinated side chain for high-performance organic thin-film transistors, *RSC Adv.*, 2016, **6**, 29164–29171.
23 X. Chen, Z. Zhang, Z. Ding, J. Liu and L. Wang, Diketopyrrolopyrrole-based Conjugated Polymers Bearing Branched Oligo(Ethylene Glycol) Side Chains for Photovoltaic Devices, *Angew. Chem.*, 2016, **128**, 10532–10536.
24 C. Lim, Y. Kim, S. Lee, H. H. Park, N. J. Jeon and B. J. Kim, Oligo(ethylene glycol)-incorporated hole transporting polymers for efficient and stable inverted perovskite solar cells, *J. Mater. Chem. A*, 2023, **11**, 6615–6624.
25 H. D. Pham, H. Hu, K. Feron, S. Manzhos, H. Wang, Y. M. Lam and P. Sonar, Thienylvinylenethienyl and Naphthalene Core Substituted with Triphenylamines—Highly Efficient Hole Transporting Materials and Their Comparative Study for Inverted Perovskite Solar Cells, *Sol. RRL*, 2017, **1**, 1700105.
26 J. Tan, J. Zhang, H. Sun, K. Chen, X. Gao, P. Zhang, C. Zhong, F. Wu, Z. Li and L. Zhu, Dopant-Free Hole Transport Material Based on Non-Covalent Interaction for Efficient Perovskite Solar Cells, *Small*, 2024, **20**, 2407027.
27 J. Ren, J. Qu, J. Chen, Z. Li, Y. Cui, H. Wang, Z. Yu and Y. Hao, Fluorinated dopant-free hole-transporting material for efficient and stable perovskite solar cells with carbon cathode, *J. Power Sources*, 2018, **401**, 29–36.
28 K. Yang, Q. Liao, J. Huang, Z. Zhang, M. Su, Z. Chen, Z. Wu, D. Wang, Z. Lai, H. Y. Woo, Y. Cao, P. Gao and X. Guo, Intramolecular Noncovalent Interaction-Enabled Dopant-Free Hole-Transporting Materials for High-Performance Inverted Perovskite Solar Cells, *Angew. Chem., Int. Ed.*, 2022, **61**, e202113749.
29 N. Yang, Y. Cui, T. Zhang, C. An, Z. Chen, Y. Xiao, Y. Yu, Y. Wang, X.-T. Hao and J. Hou, Molecular Design of Fully Nonfused Acceptors for Efficient Organic Photovoltaic Cells, *J. Am. Chem. Soc.*, 2024, **146**, 9205–9215.
30 Y. Lin, Y. Li and X. Zhan, Small molecule semiconductors for high-efficiency organic photovoltaics, *Chem. Soc. Rev.*, 2012, **41**, 4245–4272.
31 W. Xie, B. Li, X. Cai, M. Li, Z. Qiao, X. Tang, K. Liu, C. Gu, Y. Ma and S.-J. Su, Thiophene Disubstituted Benzothiadiazole Derivatives: An EffectivePlanarization Strategy Toward Deep-Red to Near-Infrared (NIR) OrganicLight-Emitting Diodes, *Front. Chem.*, 2019, **7**, 276.
32 L. Li, J. Li, L. Guo, Y. Xu, Y. Bi, Y. Pu, P. Zheng, X.-K. Chen, Y. Wang and C. Li, A multi-resonance emitter with five-membered thiophene as the π-core enables efficient, narrowband and reduced efficiency roll-off OLEDs, *Chem. Sci.*, 2024, **15**, 11435–11443.
33 M. Zhai, M. Li, Z. Deng, R. Yao, L. Wang, C. Chen, H. Wang, X. Ding, L. Liu, X. Li and M. Cheng, Perovskite Solar Cells and Modules Employing Facile Synthesis and Green-Solvent-Processable Organic Hole Transport Materials, *ACS Energy Lett.*, 2023, **8**, 4966–4975.
34 F. Zhang, C. Yi, P. Wei, X. Bi, J. Luo, G. Jacopin, S. Wang, X. Li, Y. Xiao, S. M. Zakeeruddin and M. Grätzel, A Novel Dopant-Free Triphenylamine Based Molecular ''Butterfly'' Hole-Transport Material for Highly Efficient and Stable Perovskite Solar Cells, *Adv. Energy Mater.*, 2016, **6**, 1600401.
35 R. Nakar, F. J. Ramos, C. Dalinot, P. S. Marques, C. Cabanetos, P. Leriche, L. Sanguinet, M. Kobeissi, P. Blanchard, J. Faure-Vincent, F. Tran-Van, N. Berton, J. Rousset and B. Schmaltz, Cyclopentadithiophene and Fluorene Spiro-Core-Based Hole-Transporting Materials for Perovskite Solar Cells, *J. Phys. Chem. C*, 2019, **123**, 22767–22774.
36 J. Zhang, B. Xu, M. B. Johansson, N. Vlachopoulos, G. Boschloo, L. Sun, E. M. J. Johansson and A. Hagfeldt, Strategy to Boost the Efficiency of Mixed-Ion Perovskite Solar Cells: Changing Geometry of the Hole Transporting Material, *ACS Nano*, 2016, **10**, 6816–6825.
37 X. Sallenave, M. Shasti, E. H. Anaraki, D. Volyniuk, J. V. Grazulevicius, S. M. Zakeeruddin, A. Mortezaali, M. Grätzel, A. Hagfeldt and G. Sini, Interfacial and bulk properties of hole transporting materials in perovskite solar cells: spiro-MeTAD versus spiro-OMeTAD, *J. Mater. Chem. A*, 2020, **8**, 8527–8539.
38 N. J. Jeon, H. Na, E. H. Jung, T.-Y. Yang, Y. G. Lee, G. Kim, H.-W. Shin, S. Il Seok, J. Lee and J. Seo, A fluorene-terminated hole-transporting material for highly efficient and stable perovskite solar cells, *Nat. Energy*, 2018, **3**, 682–689.
39 R. De, J. De, S. Prasad Gupta, I. Bala, Ankita, Tarun, U. Kumar Pandey and S. Kumar Pal, Oxadiazole-integrated heterocoronene discotics as ambipolar organic semiconductors, *J. Mater. Chem. C*, 2023, **11**, 980–985.
40 P. Kumar Kodali, S. Choppella, Ankita, D. Kumar, U. Kumar Pandey, M. Kumar Ravva and S. Prakash Singh, Ambipolar macrocycle derived from spiro-xanthene and carbazole: synthesis, structure–property relationships, electronic properties and host–guest investigation, *Chem. Commun.*, 2024, **60**, 11726–11729.
41 L. Nakka, Y. Cheng, A. G. Aberle and F. Lin, Analytical Review of Spiro-OMeTAD Hole Transport Materials: Paths Toward Stable and Efficient Perovskite Solar Cells, *Adv. Energy Sustain. Res.*, 2022, **3**, 2200045.

42 F. M. Rombach, S. A. Haque and T. J. Macdonald, Lessons learned from spiro-OMeTAD and PTAA in perovskite solar cells, *Energy Environ. Sci.*, 2021, **14**, 5161–5190.
43 R. D. Chavan, B. Bończak, J. Kruszyńska, A. Mahapatra, M. Ans, J. Nawrocki, K. Nikiforow, P. Yadav, J. Paczesny, F. Sadegh, M. Unal, S. Akin and D. Prochowicz, Molecular Engineering of Azahomofullerene-based ElectronTransporting Materials for Efficient and Stable Perovskite Solar Cells, *Chem.Mater.*, 2023, **35**(19), 8309–8320.
44 I. E. Castelli, J. M. García-Lastra, K. S. Thygesen and K. W. Jacobsen, Bandgap calculations and trends of organometal halide perovskites, *APL Mater.*, 2014, **2**, 081514.
45 K. Yadav, P. Kumar Behera, Ankita, Tarun, R. D. Chavan, P. Yadav, A. Ammathnadu Sudhakar and U. Kumar Pandey, Columnar self-assembled heteroatom bay-annulated perylene bisimide as passivating layer for high performance perovskite solar cells, *Sol. Energy*, 2024, **278**, 112762.
46 J. Manit, P. Kanjanaboos, P. Naweephattana, A. Naikaew, L. Srathongsian, C. Seriwattanachai, R. Supruangnet, H. Nakajima, U. Eiamprasert and S. Kiatisevi, Towards device stability of perovskite solar cells through low-cost alkyl-terminated SFX-based hole transporting materials and carbon electrodes, *Sci. Rep.*, 2024, **14**, 24167.
47 R. S. Sanchez and E. Mas-Marza, Light-induced effects on Spiro-OMeTAD films and hybrid lead halide perovskite solar cells, *Sol. Energy Mater. Sol. Cells*, 2016, **158**, 189–194.
48 L. Hajikhanmirzaei, H. Shahroosvand, B. Pashaei, G. D. Monache, M. K. Nazeeruddin and M. Pilkington, A cost-device efficiency balanced spiro based hole transport material for perovskite solar cells, *J. Mater. Chem. C*, 2020, **8**, 6221–6227.
49 Vibha, S. Sanghi, A. Agarwal, M. Chauhan, E. Arya, A. Kumari, S. Kaushik and P. Sharma, Crystal structure determination, XRD peak profile analysis and morphological study of double perovskite SrNdFeTiO6, *Mater. Today Proc.*, 2023, **82**, 79–84.
50 F. Ren, H. Xiang, K. Zhao and C. Liu, Impacts of PbI2 on high-efficiency perovskite solar cells: exploring intercalation orientations and defects, *J. Mater. Chem. C*, 2023, **11**, 13281–13289.
51 J. Han, R. H. Kim, S. Huang, J. Kim and J. S. Yun, Green Solution Processing of Halide Perovskite Solar Cells: Status and Future Directions, *Sol. RRL*, 2024, **8**, 2400262.
52 M. Abdel-Shakour, T. H. Chowdhury, K. Matsuishi, Y. Moritomo and A. Islam, Chemical passivation of the under coordinated Pb2+ defects in inverted planar perovskite solar cells via β-diketone Lewis base additives, *Photochem. Photobiol. Sci.*, 2021, **20**, 357–367.
53 R. Chetri, D. Devadiga and T. N. Ahipa, A review on 4,4′-Dimethoxydiphenylamines bearing carbazoles as hole transporting materials for highly efficient perovskite solar cell, *Sol. Energy*, 2024, **278**, 112791.
54 U. K. Pandey, A. Sharma, P. K. Behera, K. Yadav, Tarun, P. Yadav and A. A. Sudhakar, Anti-Naphthalene Bisbenzimidazole Columnar Mesogens as Interfacial Modifiers in Perovskite Solar Cells, *J. Mater. Chem. C*, 2026, DOI: **10.1039/D5TC03553H**.
55 S. N. Afraj, D. Zheng, A. Velusamy, W. Ke, S. Cuthriell, X. Zhang, Y. Chen, C. Lin, J.-S. Ni, M. R. Wasielewski, W. Huang, J. Yu, C.-H. Pan, R. D. Schaller, M.-C. Chen, M. G. Kanatzidis, A. Facchetti and T. J. Marks, 2,3-Diphenylthieno[3,4-b]pyrazines as Hole-Transporting Materials for Stable, High-Performance Perovskite Solar Cells, *ACS Energy Lett.*, 2022, **7**, 2118–2127.
56 B. Pashaei, S. Bellani, H. Shahroosvand and F. Bonaccorso, Molecularly engineered hole-transport material for low-cost perovskite solar cells, *Chem. Sci.*, 2020, **11**, 2429–2439.
57 J. Burschka, F. Kessler, M. K. Nazeeruddin and M. Grätzel, Co(III) Complexes as p-Dopants in Solid-State Dye-Sensitized Solar Cells, *Chem. Mater.*, 2013, **25**, 2986–2990.
58 M. M. Byranvand and M. Saliba, Defect Passivation of Perovskite Films for Highly Efficient and Stable Solar Cells, *Sol. RRL*, 2021, **5**, 2100295.
59 G. Maddala, R. Gade, J. Ahemed, S. Kalvapalli, N. B. Simhachalam, P. Chetti, S. Pola and R. Mitty, Efficient, dopant free phenazine based hole transporting materials for high performance perovskite solar cells, *Sol. Energy*, 2021, **226**, 501–512.
60 T. Shen, Y. Zhan and L. Shi, Time-Resolved Spectroscopy for the Study of Perovskite, *Chin. J. Electron.*, 2022, **31**, 1053–1071.
61 V. M. Le Corre, Space-Charge-Limited Current Measurements: A Problematic Technique for Metal Halide Perovskites, *J. Phys. Chem. Lett.*, 2024, **15**, 10001–10008.
62 X. Jiang, D. Wang, Z. Yu, W. Ma, H.-B. Li, X. Yang, F. Liu, A. Hagfeldt and L. Sun, Molecular Engineering of Copper Phthalocyanines: A Strategy in Developing Dopant-Free Hole-Transporting Materials for Efficient and Ambient-Stable Perovskite Solar Cells, *Adv. Energy Mater.*, 2019, **9**, 1803287.
63 S. Wang, S. Zhang, X. Shi, C. Yao, D. Jin, D. Gu, Y. Chen, J. Xu, J. Xue and R. Wang, Self-cleaning Spiro-OMeTAD via multimetal doping for perovskite photovoltaics, *Nat. Commun.*, 2025, **16**, 4167.
64 M. Sajedi Alvar, P. W. M. Blom and G.-J. A. H. Wetzelaer, Space-charge-limited electron and hole currents in hybrid organic-inorganic perovskites, *Nat. Commun.*, 2020, **11**, 4023.
65 V. M. Le Corre, E. A. Duijnstee, O. El Tambouli, J. M. Ball, H. J. Snaith, J. Lim and L. J. A. Koster, Revealing Charge Carrier Mobility and Defect Densities in Metal Halide Perovskites via Space-Charge-Limited Current Measurements, *ACS Energy Lett.*, 2021, **6**, 1087–1094.
66 B. Meng, H. Song, X. Chen, Z. Xie, J. Liu and L. Wang, Replacing Alkyl with Oligo(ethylene glycol) as Side Chains of Conjugated Polymers for Close π–π Stacking, *Macromolecules*, 2015, **48**, 4357–4363.
67 Y. Yang, Z. Liu, G. Zhang, X. Zhang and D. Zhang, The Effects of Side Chains on the Charge Mobilities and Functionalities of Semiconducting Conjugated Polymers beyond Solubilities, *Adv. Mater.*, 2019, **31**, 1903104.

68 M. T. Khan, N. H. Hemasiri, S. Kazim and S. Ahmad, Decoding the charge carrier dynamics in triple cation-based perovskite solar cells, *Sustain*, *Energy Fuels*, 2021, **5**, 6352–6360.

69 E. Berger, J. Wiktor and A. Pasquarello, Low-Frequency Dielectric Response of Tetragonal Perovskite CH3NH3PbI3, *J. Phys. Chem. Lett.*, 2020, **11**, 6279–6285.

70 M. Warish, G. Jamwal, Z. Aftab, N. Bhatt and A. Niazi, Effect of Trap States, Ion Migration, and Interfaces on Carrier Transport in Single-Crystal, Polycrystalline, and Thick Film Devices of Halide Perovskites CH3NH3PbX3 (X = I, Br, Cl), *ACS Appl. Electron. Mater.*, 2023, **5**, 5432–5445.

71 S. Sandhu and N.-G. Park, Methodologies to Improve the Stability of High-Efficiency Perovskite Solar Cells, *Acc. Mater. Res.*, 2024, **5**, 1544–1557.

72 N. Eguchi, T. Fukazawa, H. Kanda, K. Yamamoto, T. Miyake and T. N. Murakami, Performance optimization of perovskite solar cells with an automated spin coating system and artificial intelligence technologies, *EES Sol.*, 2025, **1**, 320–330.

73 B. T. Feleki, C. H. L. Weijtens, M. M. Wienk and R. A. J. Janssen, Thin Thermally Evaporated Organic Hole Transport Layers for Reduced Optical Losses in Substrate-Configuration Perovskite Solar Cells, *ACS Appl. Energy Mater.*, 2021, **4**, 3033–3043.

74 P. N. A. Fahsyar, N. A. Ludin, N. F. Ramli, P. I. Zulaikha, S. Sepeai and A. S. H. Md Yasir, Stabilizing high-humidity perovskite solar cells with MoS2 hybrid HTL, *Sci. Rep.*, 2023, **13**, 11996.

75 Y. Gao, J. Deng, Y. Che, X. Li, Y. Li, X. Wang, Z. Liao, L. Yang and J. Zhang, Ion-Exchange Polymer Network Enhanced Interfacial Compatibility for Stable and Efficient Inverted Perovskite Solar Cells, *ACS Appl. Mater. Interfaces*, 2024, **16**, 30097–30106.

76 S. Tammireddy, M. N. Lintangpradipto, O. Telschow, M. H. Futscher, B. Ehrler, O. M. Bakr, Y. Vaynzof and C. Deibel, Hysteresis and Its Correlation to Ionic Defects in Perovskite Solar Cells, *J. Phys. Chem. Lett.*, 2024, **15**, 1363–1372.

77 R. Li, P. Wang, B. Chen, X. Cui, Y. Ding, Y. Li, D. Zhang, Y. Zhao and X. Zhang, NiOx/Spiro Hole Transport Bilayers for Stable Perovskite Solar Cells with Efficiency Exceeding 21%, *ACS Energy Lett.*, 2020, **5**, 79–86.

78 A. Guerrero, J. Bisquert and G. Garcia-Belmonte, Impedance Spectroscopy of Metal Halide Perovskite Solar Cells from the Perspective of Equivalent Circuits, *Chem. Rev.*, 2021, **121**, 14430–14484.

79 Y. Sun, C. Wang, D. Zhao, J. Yu, X. Yin, C. R. Grice, R. A. Awni, N. Shrestha, Y. Yu, L. Guan, R. J. Ellingson, W. Tang and Y. Yan, A New Hole Transport Material for Efficient Perovskite Solar Cells With Reduced Device Cost, *Sol. RRL*, 2018, **2**, 1700175.

80 Y. Liu, T. Xu, Z. Xu, H. Zhang, T. Yang, Z. Wang, W. Xiang and S. Liu, Defect Passivation and Lithium Ion Coordination Via Hole Transporting Layer Modification for High Performance Inorganic Perovskite Solar Cells, *Adv. Mater.*, 2024, **36**, 2306982.

81 N. J. Jeon, H. G. Lee, Y. C. Kim, J. Seo, J. H. Noh, J. Lee and S. I. Seok, o-Methoxy Substituents in Spiro-OMeTAD for Efficient Inorganic–Organic Hybrid Perovskite Solar Cells, *J. Am. Chem. Soc.*, 2014, **136**, 7837–7840.

82 R. Li, M. Liu, S. K. Matta, A. Hiltunen, Z. Deng, C. Wang, Z. Dai, S. P. Russo, P. Vivo and H. Zhang, Sulfonated Dopant-Free Hole-Transport Material Promotes Interfacial Charge Transfer Dynamics for Highly Stable Perovskite Solar Cells, *Adv. Sustain. Syst.*, 2021, **5**, 2100244.

83 R. Chen, S. Liu, X. Xu, F. Ren, J. Zhou, X. Tian, Z. Yang, X. Guanz, Z. Liu, S. Zhang, Y. Zhang, Y. Wu, L. Han, Y. Qi and W. Chen, Robust hole transport material with interface anchors enhances the efficiency and stability of inverted formamidinium–cesium perovskite solar cells with a certified efficiency of 22.3%, *Energy Environ. Sci.*, 2022, **15**, 2567–2580.

84 C. Weng, T. Yang, Y. Li, J. Pan, X.-F. Zang, S. Wang, B. Cai and H. Cheng, Unlocking the full potential of spiro-OMeTAD in perovskite solar cells: towards synthetic routes, doping mechanism, degradation, and stability, *J. Mater. Chem. C*, 2026, **14**, 887–925.

85 H. Meng, X. Li, Y. Mai, P. Zhang and S. Li, Enhanced Efficiency and Stability of Triple-Cation Perovskite Solar Cells through Engineering of the Cell Interface with Phenylethylammonium Thiocyanate, *ACS Appl. Mater. Interfaces*, 2024, **16**, 69430–69438.

86 Z. Zhang, L. Qiao, K. Meng, R. Long, G. Chen and P. Gao, Rationalization of passivation strategies toward high-performance perovskite solar cells, *Chem. Soc. Rev.*, 2023, **52**, 163–195.